

Muon Simulations for Super-Kamiokande, KamLAND and CHOOZ

Alfred Tang and Glenn Horton-Smith

Physics Department, Kansas State University, Manhattan, KS 66506

Vitaly A. Kudryavtsev

Department of Physics and Astronomy, University of Sheffield, Sheffield S3 7RH, United Kingdom

Alessandra Tonazzo

APC and Université Paris 7, 75005 Paris, France

(Dated: October 17, 2018)

Muon backgrounds at Super-Kamiokande, KamLAND and CHOOZ are calculated using MUSIC. A modified version of the Gaisser sea level muon distribution and a well-tested Monte Carlo integration method are introduced. Average muon energy, flux and rate are tabulated. Plots of average energy and angular distributions are given. Implications for muon tracker design in future experiments are discussed.

I. INTRODUCTION

Muons are one of the most significant sources of background for underground experiments. An accurate and efficient numerical method to calculate the muon rate and average energy at an underground lab is indispensable for this type of research. This work was originally motivated by a need to resolve the question of the average muon energy for Daya Bay and KamLAND. Since Super-Kamiokande (Super-K) is essentially next to KamLAND and already has many publications quoting its muon rates, it easily becomes an ideal source of cross checks. At the same time, the need to understand the cosmic background at the far site of Double Chooz also arises. Muon data from the first CHOOZ experiment are subsequently made available so that comparison with simulation becomes possible. Given the diversity of the experimental sites being discussed, some effort is made to present the analysis in a more general context. It is hoped that the method presented here will be useful to a larger community.

The muon rate can be measured in an experiment by a number of methods. Measurement of muon energy on the other hand is quite difficult. Since a measurement made in one site under a certain hill profile is unlikely to be transferable to another site, an economical calculational method is the only practical solution. For these reasons, whenever the average muon energy is needed for the calculation of cosmogenic background rate, accurate Monte Carlo simulation is often the most reasonable alternative. Traditionally there have been some discrepancies in various reports regarding muon rate and average energy for both Super-K and KamLAND. For example, different values of muon rates have been reported by different collaborators of Super-K such as 1.88 Hz [1], 2.2 Hz [2], 2.5 Hz [3] and 3 Hz [4]. Some of these discrepancies are due to the differences of detector regions or different selection criteria used in making various cuts. For example, a cut at 1.6 GeV is made to eliminate the muon background in the study of the upward throughgoing muons in Reference [2]. This cut has the effect of lowering the cosmic muon rate. In Reference [3], the 2.5 Hz cosmic muon rate quoted is an estimate used to make the spallation cut. Differences in cosmic muon rates due to the differences in detector regions will be analyzed by simulation studies later. As far as KamLAND is concerned, accurate simulations of the average muon energy, flux and rate are presently needed to aid the data analysis process. In addition, the design of muon tracker systems for future experiments depend on detailed simulations that can handle complicated topography. In an effort to build a reliable tool for all these needs, this paper introduces a complete numerical method from the ground up—beginning with an improved Gaisser sea level muon parameterization, showing in detail the logic of the numerical method, making mention of useful numerical tools and ending with numerous cross checks with experimental data including those of ground level muons.

II. A BOTTOM-UP DESIGN

A. Preliminaries

The goal of this section is to lay the theoretical foundation for how to incorporate MUSIC with a user-supplied sampling algorithm. Details of the implementation of the numerical method outlined in this section can be found in Appendix A. MUSIC is a FORTRAN subroutine that simulates the 3-dimensional transport of muons through a slant depth X of a material taking into account energy loss due to ionization, pair production, Bremsstrahlung and inelastic scattering [5, 6]. MUSIC is composed of two main parts—(1) the Monte Carlo simulation of muon energy loss and (2)

the Monte Carlo simulation of angular deviation and lateral displacement. In order to distinguish quantities related to initial muons on the surface and the final muons that survive at a certain depth underground, the subscripts μ_0 and μ will be used to denote the two types of muons respectively.

The testing of the present numerical method involves the comparison of the simulated results against published experimental and simulated data. The most convenient item of comparison is the vertical muon intensity $I_\mu^v(h)$ versus vertical depth h underneath a flat surface in standard rock because of the abundance of experimental data. In order to set the stage for the following discussions, several conventional quantities are defined in the beginning. For instance, θ is defined to be the zenith angle of the line of sight of the muons and ϕ is the azimuthal angle of the same, measured from the easterly direction in the counter-clockwise sense. Directional muon intensity $I_\mu(h, \cos \theta)$ has units of $\text{cm}^{-2} \text{sr}^{-1} \text{s}^{-1}$. Vertical muon intensity is taken as

$$I_\mu^v(h) = I_\mu(h, \cos \theta = 1), \quad (1)$$

which also has the unit of $\text{cm}^{-2} \text{sr}^{-1} \text{s}^{-1}$. Integrated muon intensity is defined as [7]

$$J_\mu(h) = \int_{\Omega} I_\mu(X, \cos \theta) d\Omega, \quad (2)$$

where Ω defines the solid angle coverage and the slant depth X is the distance traveled by the muon in rock. The argument X in $I_\mu(X, \cos \theta)$ is generally a function of $\cos \theta$. For example, $X = h/\cos \theta$ in the case of a flat surface. The unit of integrated muon intensity is $\text{cm}^{-2} \text{s}^{-1}$.

B. Modified Gaisser Parameterization

The accuracy of the simulation depends on MUSIC, the parameterization of the surface muon intensity and the user-supplied sampling algorithm. A standard atmospheric muon parameterization is given by Gaisser [8] as

$$\frac{dN_{\mu_0}}{dE_{\mu_0}d\Omega} \simeq A \frac{0.14E_{\mu_0}^\gamma}{\text{cm}^2 \text{sr s GeV}} \left\{ \frac{1}{1 + \frac{1.1\tilde{E}_{\mu_0} \cos \theta}{115}} + \frac{.054}{1 + \frac{1.1\tilde{E}_{\mu_0} \cos \theta}{850}} + r_c \right\}. \quad (3)$$

Muon energy E_{μ_0} at the surface is measured in GeV and θ is the angle subtended between the incoming cosmic ray particle and the normal to the upper atmospheric layer. If the earth were flat, θ is also the zenith angle on the ground surface. Since the earth is not flat, a correlation needs to be made between the zenith angle on the ground surface and the angle measured on the upper atmosphere. In order to clarify the distinction between the two definitions of angle, a new symbol θ^* is invented to denote the angle measured on the upper atmosphere as a function of θ which is assigned specifically to the zenith angle on the ground surface from now on. The calculation of θ^* will be explained later. The symbols A , γ and r_c refer to the overall scale factor, power index and the ratio of the prompt muons to pions respectively. In the low energy regime, E_{μ_0} needs to be modified slightly by an energy loss through the atmosphere. The symbol \tilde{E}_{μ_0} denotes the energy of muon on top of the atmosphere. The differentials of time dt and area dA are omitted from the denominator on the left-hand-side of Eq. (3) for the sake of simplicity. The original Gaisser parameterization has $A = 1$, $\gamma = 2.70$, $\tilde{E}_{\mu_0} = E_{\mu_0}$ and $r_c = 0$. For large depth greater than 1–2 km w.e. (kilometer water equivalence), the LVD parameterization [9] is recommended. In that case, $A = 1.84$, $\gamma = 2.77$. Since this work primarily concerns simulations for relatively shallow depths as in Super-K, KamLAND and CHOOZ, the Gaisser parameterization is adequate for the high energy part ($E_{\mu_0} > (100/\cos \theta)$ GeV) of the spectrum. Since there are enough low energy muons that survive at shallow depths, rare high energy muons ($E_{\mu_0} > 10^6$ GeV) are omitted from the calculations. The valid energy range for the Gaisser parameterization is $(100/\cos \theta) < E_{\mu_0} < 10^6$ GeV and small angle $\theta < 70^\circ$ where the effect due to the curvature of the earth is negligible. In the low energy limit ($E_{\mu_0} \leq (100/\cos \theta)$ GeV), the Gaisser parameterization is significantly higher than the observed values. The expected angular dependence of $\cos^n \theta$ with $n \sim 2$ in this regime must also be taken into account. To satisfy all these additional requirements in the small E_{μ_0} and large θ regimes, the following modifications to Eq. (3) are suggested for $(1/\cos \theta^*) < E_{\mu_0} < (100/\cos \theta^*)$ GeV:

$$r_c = 10^{-4}, \quad (4)$$

$$\Delta = 2.06 \times 10^{-3} \left(\frac{950}{\cos \theta^*} - 90 \right), \quad (5)$$

$$\tilde{E}_{\mu_0} = E_{\mu_0} + \Delta, \quad (6)$$

$$A = 1.1 \left(\frac{90\sqrt{\cos \theta + 0.001}}{1030} \right)^{\frac{4.5}{E_{\mu_0} \cos \theta^*}}. \quad (7)$$

It is important to note the term involving $\cos\theta$ inside the square root of Eq. (7) does not have a star. The LVD publications set the upper limit on the ratio of prompt muons to pions to be $r_c < 2 \times 10^{-3}$ at 95% confidence level [9, 10]. However χ^2 of the fits is lower for smaller values of r_c such that the choice of Eq. (4) is justified by statistical reason. The symbol Δ in Eq. (5) has the interpretation of mean energy loss of muons in the atmosphere. The value 2.06×10^{-3} refers to the stopping power of matter against muons in units of GeV per g/cm² at $E_{\mu 0} \simeq 50$ GeV where the radiative effects reach 1% [11]. The multiplication of this value with the mean muon slant depth in the atmosphere will give the mean energy loss of muons in the atmosphere. A commonly quoted value of the atmospheric height h_F is 1000 g/cm². Reference [12] quotes a specific value of $h_F = 1030$ g/cm² along with a value of interaction length (the average distance between the point where a primary proton enters the atmosphere and the point where a muon is produced) $\lambda_N = 120$ g/cm². The atmospheric height h_F is a function of scale height h_0 which in turn is a function of temperature. In addition the stopping power used in Eq. (5) is simply a rough estimate. For these reasons, h_F should be adjusted to produce the best fit of experimental data in the low energy regime. For the purpose of constructing Δ , the choice of $h_F = 950$ g/cm² is made. Beside the aforementioned value of interaction length $\lambda_N = 120$ g/cm² quoted in Reference [12], many other values have also been quoted in the literatures, *e.g.* $\lambda_N = 77.6$ g/cm² [13] and $\lambda_N = 80$ g/cm² [14]. Again for the purpose of constructing the fits, a median value of $\lambda_N = 90$ g/cm² is chosen for Δ . Putting all these values together, the mean muon slant depth is $(950/\cos\theta^* - 90)$ g/cm² such that the final form of Eq. (5) is obtained. For low energy muons, there is a slight difference, Δ , between the muon energy at ground level $E_{\mu 0}$ and the muon energy on top of the atmosphere $\tilde{E}_{\mu 0}$. Since the critical energy (the threshold by which the mechanism changes from radiation losses to ionization losses) used in Eq. (3) refers to $\tilde{E}_{\mu 0}$, an adjustment is needed for the low energy regime as given in Eq. (6). The meaning of Eq. (7) is essentially the multiplication of an effective factor of 1.1 due to the nuclear enhancement of multiplicity [12] and the probability of muon decay S_μ . The form of S_μ used in Eq. (7) is similar to that in Reference [12] and can easily be derived as follows: the decay probability is related to decay length $L = -v\gamma\tau \ln R$ such that $S_\mu = \exp(-\lambda_F/L)$ where $\lambda_F \equiv h_F/\cos\theta^*$ is the slant height of the atmosphere, v is muon velocity, $\gamma \equiv 1/\sqrt{1-v^2}$ is the Lorentz factor, τ is the muon lifetime and $0 \leq R \leq 1$ is a uniformly distributed number [15]. In the muon energy regime $E_{\mu 0} > (1/\cos\theta^*)$ GeV, the approximation $v \simeq 1$ is acceptable. Furthermore, if the choice of $R = \lambda_N/\lambda_F$ is made along with the standard substitutions $\gamma = E_{\mu 0}/m_\mu$ and $h_F m_\mu/\tau \simeq 1.04$ GeV, the original form of S_μ in Reference [12] is recovered. This derivation reveals that the form of S_μ in Reference [12] does not incorporate any matter and geomagnetic effects which may be important for low energy muons. In the present work, nonlinear effects are taken into consideration by assuming a modification to the decay length to achieve the best fits of experimental data such that

$$\tilde{L} \equiv 0.231 \ln \left(\frac{\sqrt{\cos\theta + 0.001}}{\cos\theta^*} \right) L. \quad (8)$$

At this point, Eq. (8) is purely phenomenological. There is no simple physical explanation for this change other than the fact that it fits the low energy muon data. By replacing L with \tilde{L} in Eq. (8) and repeating the derivation of S_μ above, Eq. (7) is obtained.

The modifications in Eqs. (4)–(7) alone cannot fit the data in the lowest energy range. For $E_{\mu 0} \leq 1/\cos\theta^*$ GeV, the basic form of the parameterization is the same as Eqs. (3)–(7) with the exception that the substitution

$$E_{\mu 0} \rightarrow \frac{3E_{\mu 0} + 7 \sec\theta^*}{10} \quad (9)$$

is made before $E_{\mu 0}$ is passed to Eqs. (3)–(7). The substitution in Eq. (9) is just another phenomenological tool to achieve good fits with experimental data.

The value of $\cos\theta^*$ is sometimes calculated using a simple geometrical extrapolation assuming that the altitude of first interaction is known *a priori*. The present work takes a different approach by using a more complicated extrapolation method described in Reference [16] that shows how $\cos\theta^*$ can be extracted from an integral equation by equating interaction length $X(\theta) = X(0)$. In essence the formula below taken from Reference [16] parameterizes the numerical solution of the integral equation:

$$\cos\theta^* = \sqrt{\frac{x^2 + p_1^2 + p_2 x^{p_3} + p_4 x^{p_5}}{1 + p_1^2 + p_2 + p_4}}, \quad (10)$$

where $x \equiv \cos\theta$, $p_1 = 0.102573$, $p_2 = -0.068287$, $p_3 = 0.958633$, $p_4 = 0.0407253$ and $p_5 = 0.817285$. The terms involving $\cos\theta$ in Eq. (3) must be replaced by $\cos\theta^*$ for consistency. Eq. (7) is protected against division by zero because $\cos\theta^* \geq 0.103458$ for $\cos\theta \geq 0$ according to Eq. (10). The modified Gaisser parameterization is based on the world data set and hence represent an average of the global sea level muon distribution. The geomagnetic field

affects only the low energy spectrum, typically below 2 GeV for integrated muon intensity [17] and approximately less than 20 GeV for vertical muon intensity [18]. The east-west effect is also shown to be negligible at ground level [19] by careful simulations. For the purpose of calculating the muon overburden deep underground, geomagnetic effects can be ignored because low energy sea level muons will not survive through rock by default. In essence, the present parameterization is composed of the union of 3 segments: $E_{\mu 0} > (100/\cos\theta^*)$ GeV (the standard Gaisser formula), $(1/\cos\theta^*) < E_{\mu 0} \leq (100/\cos\theta^*)$ GeV (Eqs. (4)–(7)) and $E_{\mu 0} \leq (1/\cos\theta^*)$ GeV (Eq. (9)). Figure 1 illustrates the quality of the fits between the modified Gaisser formula and experimental data. The goodness of fit tends to degrade only at very large angles ($\theta > 85^\circ$). The worst disagreement between experimental data and the parameterization in those cases is about 40%. However the worst case scenario of the 40% disagreement occurs only at low energy ($E_{\mu 0} < 10$ GeV) and a relatively small sector at large angles ($\theta > 85^\circ$) so that the integrated spectrum is dominated by the very accurate parts of the parameterization at smaller angles. Finally it should be emphasized that the modifications to the low energy part of the standard Gaisser formula outlined in Eqs. (4)–(7) and (9) will not have any significant impact on the simulations of deep underground experiments. Nevertheless an accurate description of the low energy part of the sea level muon distribution is important for calculating the muon overburden for sites situated at shallow depths such as the near sites of the Double Chooz and Daya Bay experiments.

C. Modeling Physical Observables

Directional intensity at depth h is obtained by integrating the Gaisser parametrization and the muon survival probability over the initial muon energy $E_{\mu 0}$ at the surface as

$$I_\mu(X, \cos\theta^*, \phi) = \int_0^\infty dE_{\mu 0} P(E_{\mu 0}, X, \theta^*, \phi) \frac{dN_{\mu 0}(E_{\mu 0}, \cos\theta^*)}{dE_{\mu 0} d\Omega}. \quad (11)$$

The probability function $P(E_{\mu 0}, X, \theta^*, \phi)$ defines the survival probability of a muon with initial energy $E_{\mu 0}$ traversing a slant depth X from the zenith angle θ^* and the azimuthal angle ϕ . It is emphasized that the symbol I_μ as used in this paper has a different meaning than I_μ in Reference [31] in that the latter refers to a differential muon intensity containing a probability distribution function $P(E_\mu, E_{\mu 0}, X, \theta^*, \phi)$ which is related to $P(E_{\mu 0}, X, \theta^*, \phi)$ as per

$$P(E_{\mu 0}, X, \theta^*, \phi) \equiv \int dE_\mu P(E_\mu, E_{\mu 0}, X, \theta^*, \phi). \quad (12)$$

In Reference [31], 2×10^7 muons with energies from 0.1 up to 1000 TeV were propagated through 15 km.w.e. of rock. The values of $P(E_\mu, E_{\mu 0}, X)$ were stored and then integrated numerically using an equation similar to Eq. (11) to obtain energy and angular distributions at any particular depth. This work takes a different approach by evaluating $P(E_{\mu 0}, X, \theta^*, \phi)$ *in situ* in the Monte Carlo integration. This approach requires a smaller number of simulated events (typically 5×10^6) and is more versatile when applied to arbitrary hill profiles when $P(E_{\mu 0}, X, \theta^*, \phi)$ must be re-evaluated every time the (x, y) -coordinates are changed. In principle the transport of muons from the surface to a point underground and vice versa are equivalent as far as the calculation of energy loss is concerned. The most important requirement of the present method is the uniform generation of $E_{\mu 0}$, θ and ϕ as shown in Appendix A. An arbitrary energy dependent observable $\mathcal{O}_\mu(E_\mu)$ can be estimated as

$$\langle \mathcal{O}_\mu(X, \cos\theta^*, \phi) \rangle = \frac{1}{I_\mu(X, \cos\theta^*, \phi)} \int_0^\infty dE_{\mu 0} \frac{dN_{\mu 0}(E_{\mu 0}, \cos\theta^*)}{dE_{\mu 0} d\Omega} \int_0^\infty dE_\mu \mathcal{O}_\mu(E_\mu) P(E_\mu, E_{\mu 0}, X, \theta^*, \phi). \quad (13)$$

The bracketed quantity on the left-hand-side of Eq. (13) represents the average of \mathcal{O}_μ . The bracket will be dropped from now on for the sake of simplicity unless ambiguities arise due to the choice of symbols. With Eqs. (11) and (13), vertical intensity and average energy are

$$I_\mu^v(h) = \int_0^\infty dE_{\mu 0} P(E_{\mu 0}, h, \theta^* = 0, \phi) \frac{dN_{\mu 0}(E_{\mu 0}, \cos\theta^* = 1)}{dE_{\mu 0} d\Omega}, \quad (14)$$

$$E_\mu^v(h) = \frac{1}{I_\mu^v(h)} \int_0^\infty dE_{\mu 0} \frac{dN_{\mu 0}(E_{\mu 0}, \cos\theta^* = 1)}{dE_{\mu 0} d\Omega} \int_0^\infty dE_\mu E_\mu P(E_\mu, E_{\mu 0}, h, \theta^* = 0, \phi). \quad (15)$$

There are many different ways to implement Eqs. (14) and (15) numerically. Appendix A describes an efficient and accurate Monte Carlo method. Simulated values of $I_\mu^v(h)$ beneath a flat surface are compared against experimental and simulated data in Figures 2. The results obtained by using the modified Gaisser parameterization incorporating

Eqs. (4)–(7) at low energy agrees with experimental data more closely than those using the standard Gaisser parameterization only. Figure 3 shows the consistency between simulated and experimental data at shallow depths. (The interpretation of Figure 3 will be discussed more fully in Appendix A.) The integrated muon intensity and average energy are

$$J_\mu = \int_\Omega d\Omega \int_0^\infty dE_{\mu 0} P(E_{\mu 0}, X, \theta^*, \phi) \frac{dN_{\mu 0}(E_{\mu 0}, \cos \theta^*)}{dE_{\mu 0} d\Omega}, \quad (16)$$

$$\langle E_\mu \rangle = \frac{1}{J_\mu} \int_S d\Omega \int_0^\infty dE_{\mu 0} \frac{dN_{\mu 0}(E_{\mu 0}, \cos \theta^*)}{dE_{\mu 0} d\Omega} \int_0^\infty dE_\mu E_\mu P(E_\mu, E_{\mu 0}, X, \theta^*, \phi). \quad (17)$$

J_μ and $\langle E_\mu \rangle$ in Eqs. (16) and (17) are functions of the location of the point of sampling underneath a topographic profile. The arguments of these functions, namely the coordinates of the point of sampling, are understood and therefore not displayed explicitly. The brackets around E_μ on the left-hand-side of Eq. (17) are dropped in the following text whenever the reference to average muon energy is clear from the context of the discussion. Integrated intensity can be computed in a similar way as vertical intensity. The only difference is that the depth X is now a function of θ and ϕ . In the case of a flat surface, the relation takes on a simple form $X = h/\cos \theta$. In the case of an arbitrary hill profile, there is no longer any simple relationship among X , θ and ϕ .

The key of the present numerical method is uniform generation of integration variables which can be achieved in reliable ways through various uniform generation algorithms such as the CERNLIB routine RANLUX. The logic of the method is relatively simple so that there is little ambiguity of its correctness. All these observations lead to the conclusion that MUSIC is sufficiently accurate over the relevant range of muon energy. Simulated integrated muon intensity and average energy are compared against published simulations in Table I.

III. PREPARING THE CALCULATION

A. Digital Maps

The starting point of a muon simulation over an arbitrary hill profile is the digital map of the surrounding topology. The accuracy of a digital map directly affects the accuracy of the calculation so that a detailed knowledge of the hill profile is important. According to a contour map published in Reference [33], KamLAND is separated from Super-K by 187m and its bearing is N66.6E with respect of Super-K. The top of the Super-K tank and the bottom of the KamLAND tank are situated at 350m above sea level. Both sites are almost directly underneath the peak of Ikenoyama at 1.35 km. Due to their proximity, both sites have very similar muon energy and flux. However the sizes of the two detectors are vastly different so that their muon rates scale accordingly. The digital map of the Ikenoyama mountain profile around Super-K is extracted from a code used by M. Nakahata originally to calculate the muon background for Super-K. The Super-K digital map sets its origin at the location of the detector and parameterizes coordinates in terms of (ρ, ϕ, h) . This particular format does not allow a simple coordinate transformation of the origin from Super-K to KamLAND. As a result, the digital map of KamLAND is constructed independently from a contour map for this work. In order to guarantee a sufficient solid angle coverage for the simulation, both digital maps cover circular areas of radius 3950 m. The topological map of CHOOZ is generated from a 2D contour map using a shareware called **3DField** [34]. A visualization of the digital map over the Ardennes Mountains is shown in Figure 4. **3DField** has the option of generating an ASCII data file containing the (x, y, z) coordinates of the latticized hill profile. One side of the CHOOZ detector is beneath a steep hill so that a large range of the solid angle coverage is parameterized by a relatively small set of lattice points. In order to increase the density of lattice points over the steep section of the Ardennes hill profile, another digital map is created over a smaller area around the detector. At the end, both digital maps are spliced together to form one single digital map so that the entire solid angle coverage is represented more evenly.

B. Detector Geometry

The calculation of the average muon rate depends on the details of the detector geometry. For Super-K, the parameters that define the geometry of the cylindrical tank are $L_0 = 41.40$ m and $R_0 = 19.65$ m. An inner volume is defined to eliminate the simulations of very small muon track lengths inside the detector geometry that do not intersect the active region of the detector. The choice of the inner volume is not critical for the calculation of muon rate inside the outer tank R_μ^t . For the purpose of this work, the inner volume used in the simulation of R_μ^t is also the inner detector volume of Super-K whose dimensions are $L = 36.20$ m and $R = 16.90$ m. The inner and outer tanks of

Super-K have almost the same aspect ratios so that the muon rate inside the inner tank R_μ^i can be obtained simply by scaling R_μ^t according to the ratio of the physical areas A_0 of the two tanks. The geometry of the cylindrical tank at KamLAND is defined by $L_0 = 19.68$ m and $R_0 = 9.50$ m. The inner spherical volume of KamLAND for the purpose of this simulation is taken to be the area bounded by the buffer region with $R = 8.25$ m. For the simulation of the muon rate inside the KamLAND detector volume, a sphere of radius $R_0 = 6.50$ m is used. In the case of CHOOZ, the cylindrical tank has the dimensions of $L_0 = 5.5$ m and $R_0 = 2.75$ m. The inner detector is filled with Gd-loaded liquid scintillator and has the shape of a short cylinder with hemispherical end caps. Muon rate inside the Gd-loaded region is not simulated in the present work.

C. Rock Composition

Chemical composition of the rock affects a MUSIC simulation in that two out of three cross section files need to be calculated with specific rock data *a priori*. Table II gives the chemical composition of the Ikenoyama and Ardennes rock. The average atomic number and weight are $\langle Z \rangle = 10.13$ and $\langle A \rangle = 20.42$ for the Ikenoyama rock and $\langle Z \rangle = 11.8$ and $\langle A \rangle = 24.1$ for the Ardennes rock. Hydrogen composition is 2.2% for Ikenoyama and negligible for Ardennes. The rock density and the radiative length are $\rho = 2.70$ g/cm³ and $\lambda = 25.966$ g/cm² for Ikenoyama and $\rho = 2.81$ g/cm³ and $\lambda = 23.3$ g/cm² for Ardennes respectively. The present simulation for CHOOZ takes the approximate chemical composition and the average rock density [35] as inputs. The Ardennes Mountains has a complicated rock density profile with a layer of dense rock (3.1 g/cm³) [36] on the northeast sector.

In principle complex geological profiles can be incorporated into the MUSIC simulation by a stratified approach in which a simulation is segmented according to regions of different densities, average atomic numbers $\langle Z \rangle$, average atomic masses $\langle A \rangle$ and radiation lengths. Although the stratified approach is possible, it may not be easily achieved in practice. Aside from the computational challenge of simulating a complex geological profile, information of the geological profile obtained by geological surveys may not be generated with sufficient details to support a realistic simulation in the first place. Fortunately the stratified approach can be avoided in many cases. If $\langle Z \rangle$ and $\langle A \rangle$ are constant and only density varies with depth, the mean density should give the same average muon energy and flux as those generated from stratified densities. Varying densities may affect the profiles of angular distributions as in the CHOOZ case shown in Section IV. Radiation length affects only the lateral displacement, which is not under investigation in this paper. Small changes in $\langle Z \rangle$ and $\langle A \rangle$ (up to 10%) should not seriously affect the muon flux as long as the mean values of all layers are found accurately. This work does not attempt to simulate the detailed geological profile of the Ardennes Mountains. It is shown in Section IV that the simulated results due to the simplification of the Ardennes geological profile are consistent with the previous CHOOZ measurements within errors and that simulated results of a uniform Ikenoyama mountain profile agree with experimental data.

IV. RESULTS AND DISCUSSIONS

A. Average Muon Rate

The calculation of muon rate depends on the the effective area of the detector. The basic strategy of calculating the effective area A is to multiply the physical area A_0 with the ensemble average of the inner products of randomly generated unit vectors \hat{r}_i pointing from an inner volume and the unit normal vectors \hat{r}_0^i pointing away from the outer surface. In this case, the ensemble average also constrains the pseudo survival probability of muons $\langle P \rangle$ that will be defined more precisely by Eq. (A14) in Appendix A. Figure 13 visualizes how the inner products are done. An intuitive way to think about the effective area A is

$$A = \frac{A_0 \langle P \rangle}{N} \sum_{i=1}^N \hat{r}_i \cdot \hat{r}_{0i}. \quad (18)$$

In the case of a cylindrical detector, the physical area is $A_0 = \pi R_0^2 + 2\pi R_0 L_0$. Similarly $A_0 = 4\pi R_0^2$ for a spherical detector and so on. If Eq. (18) is used, the average muon rate R_μ is simply

$$R_\mu = J_\mu A. \quad (19)$$

The average muon flux J_μ is always sampled at the center of the detector volume in this work. Although the macroscopic strategy defined by Eqs. (18) and (19) gives reasonable results, a microscopic strategy to compute the

muon rate is considered more accurate, namely

$$R_\mu = \int d\mathbf{A} \cdot \hat{r} \int_\Omega d\Omega \int_0^\infty dE_{\mu 0} P(E_{\mu 0}, X, \theta^*, \phi) \frac{dN_{\mu 0}(E_{\mu 0}, \cos \theta^*)}{dE_{\mu 0} d\Omega}, \quad (20)$$

where $d\mathbf{A}$ is a differential area element along the detector wall and \hat{r} is a unit vector along the muon line of sight. Both are functions of position along the detector wall, $\cos \theta^*$ and ϕ . Appendix A gives a numerical implementation of Eq. (20).

Table III summarizes the main results in terms of average muon energy, flux and rate. The muon rate in the outer tank of Super-K generated by the present method is somewhere between the experimental values published in References [3] and [2]. The 3 Hz muon rate quoted in Reference [4] is most likely a rounded figure. It is not clear if the 1.88 Hz muon rate in Reference [1] refers to the inner detector volume only. If so, it would agree with the simulated result very closely. The muon rate at Kamiokande is usually quoted as 0.44 Hz [37]. Since KamLAND is slightly larger than Kamiokande, the muon rate should be scaled according the ratio of the physical areas A_0 of the two tanks which becomes approximately 0.5 Hz. The unofficial measured rates on the KamLAND outer detector and the balloon are 0.75 and .21 Hz respectively. They differ from the simulated results by about 10% and 17% respectively. The official measured muon rate in the spherical buffer region of radius $R_0 = 8.25$ m is 0.34 Hz [38] and the simulated result is 0.396 Hz (14% difference). The muon flux of $0.4 \text{ m}^{-2} \text{ s}^{-1}$ quoted by CHOOZ [36] is smaller than the simulated exact result by about 35%, which is attributable to the single digit of precision of the quoted rate and the approximated geology used in our simulation. The errors in the simulated results in Table III are a combination of the systematic error from map-making and the statistical error from the Monte Carlo simulation. The systematic error of the mountain profile coming from the calculation of the scale that relates physical distance on the contour map to the relative distance on the digital map is taken to be 0.5%. The systematic errors of E_μ , J_μ and R_μ are calculated by varying the slant depth X by 0.5% before passing it to MUSIC. The statistical variance is calculated in the usual way by varying the random seed.

B. Energy and Angular Distributions

The energy distribution dJ_μ/dE_μ in Figure 5 is defined by the formula

$$J_\mu \simeq \int_0^\infty dE_\mu \frac{dJ_\mu}{dE_\mu}, \quad (21)$$

and has the unit of $\text{GeV}^{-1} \text{ cm}^{-2} \text{ s}^{-1}$. Angular and double differential distributions can also be defined in similar ways. Appendix A describes numerical implementations for various types of distributions. Figure 5 plots the cosmic muon energy distributions at Super-K, KamLAND and CHOOZ. The purpose of the figure is to show the global properties of the energy distributions of various experiments. Although the distributions look smooth on the log-log scale, the fluctuations in the low energy regime ($E_\mu < 1 \text{ GeV}$) will become more apparent on the semi-log scale. Fortunately the fluctuation in the low energy part of the spectrum on the log scale is suppressed by the smallness of the Jacobian that contains a factor of E_μ so that the accuracy of the calculations of the average muon energy E_μ and flux J_μ are not affected. If the energy distribution of stopping muons is needed, generation of $E_{\mu 0}$ and $\cos \theta$ according to the surface muon distribution is recommended.

Figures 6–8 illustrate the angular distributions of muons. Experience shows that 5×10^6 simulated events are generally adequate to generate reasonably good quality distributions in most cases. The polar angle θ in the relevant plots is defined to be the zenith angle consistent with Eqs. (2) and (3). The azimuthal angle ϕ is set to zero when the final muon travels from east to west. The momentum of the final muon is opposite to the line of sight connecting the detector and the muon and is defined by θ and ϕ . The only exception to the present definition of θ and ϕ is Figure 6 because the Super-K digital map uses a different convention. Figure 9 compares the $\cos \theta$ and ϕ distributions between simulations and experiment at KamLAND. Figure 10 compares the θ and ϕ distributions between simulations and a cosmic ray experiment done on the CHOOZ site in 1994. The experiment consists of four $1 \times 1 \text{ m}^2$ PRC (Resistive Plate Chambers) plates separated from each other by 20 cm. The simulation of the experiment defines a muon event as the coincidence of any two of the RPC plates being triggered. The difference between the simulated and the experimental θ distributions can be explained by the fact that a significant number of the muons coming from the steep section of the Ardennes hill profile cannot be detected by a muon tracker composed of top and bottom horizontal plates only. In order to measure the muons coming from large zenith angles, additional trackers are needed on the sides. The remaining small differences between the simulated and experimental results and the aberrations presumably arising from the variation in geology described in Reference [36] are not simulated in this work. The difference between the simulated and experimental $dJ/d\phi$ for $0 < \phi < 150^\circ$ in Figure 10 is consistent with an unpublished result in an internal

note of the CHOOZ collaboration. Notwithstanding the lack of detailed treatment of smaller features, a macroscopic picture emerges by the way of a qualitative comparison in the performance of two types of muon trackers represented by the horizontal plate cosmic ray experiment on the CHOOZ site and the muon veto system of KamLAND. The simulated $\cos\theta$ and ϕ distributions agree well with KamLAND experimental data because the muon tracker system of KamLAND has full sensitivity over the entire range of the hemispherical solid angle. The disagreement between the exact simulation of the θ distribution and the experimental data measured by horizontal plates of the CHOOZ cosmic ray experiment in Fig. 10 shows that the contribution of muon flux from the sides cannot be neglected in the case of a detector located underneath a hilly topology. The obvious exception to this claim will be the case where a detector is situated underneath a flat surface so that the slant depth grows with $\sec\theta$.

Figures 11–12 plot the average muon energy versus θ and ϕ for KamLAND and CHOOZ respectively. It is noted that the differential flux in Figs. 9 and 10 tends to vary inversely with the average muon energy E_μ per angle in Figs. 11 and 12. This anti-correlation is intuitive in that average muon energy generally increases with slant depth while muon intensity decreases with slant depth.

V. CONCLUSION

The described method integrates MUSIC, a modified Gaisser parameterization of the sea-level muon spectrum, and a uniform sampling algorithm for the surface topography. The method is efficient, robust, and portable. Given sufficiently accurate geological data, the method is capable in principle of predicting muon rates and mean energies within a few percent accuracy for depths less than 2.5 km.w.e., as indicated by the error estimates in Table III. In practice, simulations performed using simplified geology assuming uniform rock composition lie within 10~20% of observed rates published by Super-Kamiokande and KamLAND, and within 35% of the published flux at the geologically more complex CHOOZ site. Although muon simulations for any arbitrary hill profile have already been done many times by other researchers previously, there are very few complete documents approximating a pedagogical introduction to the numerical method itself. Although muon rates can be measured in an experiment, muon energy is difficult to measure so that knowledge of the average muon energy depends on simulation. For this reason, the reliability of the numerical method is very important. In applications such as the estimation of muon background in reactor θ_{13} experiments, the method of uniform generation of variables can serve as an additional cross check for accuracy. Although the standard Gaisser or LVD parameterizations are generally adequate for the simulations of the deep underground experiments, the modified Gaisser parameterization is indispensable for shallow depth muon simulations.

Acknowledgments

The authors thank K. B. Luk, M. C. Chu, W. K. Ngai, M. Y. Guan, J. Cao, Y. F. Wang, J. Learned, J. Shirai, K. Ichimura and J. Formaggio for providing relevant information and helpful discussions. Members of the KamLAND and CHOOZ Collaborations have graciously released previously unpublished data. Special thanks go to D. Dwyer, S. Freedman, P. Decowski, L. Hsu and G. Giannini and K. Inoue on this point. A. Tang was supported by the Chinese University of Hong Kong through the postdoctoral fellowship program where part of this work was done. V. A. Kudryavtsev wishes to thank Particle Physics and Astronomy Research Council (UK) and the EU FP6 Programme ILIAS (Contract RII3-CT-2004-506222) for support. G. Horton-Smith and A. Tang are supported by the Department of Energy and the State of Kansas.

APPENDIX A: TECHNICAL DETAILS OF THE NUMERICAL METHOD

The quality of the 3D topological map is crucial for an accurate calculation of muon overburden. It is usually the first and the most important step. Care should be taken to remove the disconnected parts of the mountain profile. If a ray defined by a specific set of (θ, ϕ) passes through disconnected parts of the mountain geometry resulting in several different values of slant depth X , the smallest value of X is used for that particular solid angle.

The range of the energy in the integral goes in principle from 0 to infinity. It is more advantageous to numerically integrate over $\log E_{\mu 0}$ instead of $E_{\mu 0}$. (In this work, log refers to base 10 logarithm and ln to base e .) On the other hand, integration over $E_{\mu 0}$ will give essentially the same results. The range of numerical integration over muon energy $E_{\mu 0}$ is labeled by the lower and upper bounds, E_l and E_u respectively. This work chooses not to change the variable in such a way to integrate up to $E_{\mu 0} \rightarrow \infty$. More specifically, the natural cut-off point ought to be a sharp drop in the muon spectrum which in turn correlates with the knee of the primary proton spectrum between 1000 and 10000 TeV.

The change in the muon spectrum is 5–10 times lower than that so that a reasonable estimate of the upper limit is $E_u = 10^6$ GeV. As a practical consideration, it is more computationally efficient to set E_l not strictly as the rest mass of muon m_μ but the minimum muon energy needed to survive the minimum slant depth of a particular geographic profile so that CPU time is not wasted in simulating muons that cannot survive by default.

After the change of variables from E to $\log(E)$, Eq. (11) is transformed as

$$I_\mu(X, \cos \theta^*, \phi) \simeq \ln 10 \int_{\log E_l}^{\log E_u} d \log E_{\mu 0} P(E_{\mu 0}, X, \theta^*, \phi) E_{\mu 0} \frac{dN_{\mu 0}(E_{\mu 0}, \cos \theta^*)}{dE_{\mu 0} d\Omega}. \quad (\text{A1})$$

An integral in the Monte Carlo method [42] can be approximated as

$$\int_{y_1}^{y_2} f(x, y) dy_x \simeq \langle f(x, y) \rangle \cdot (y_2 - y_1), \quad (\text{A2})$$

where $\langle f(x, y) \rangle$ is the average of $f(x, y)$ over y . With Eqs. (A1) and (A2), Eq. (11) can be calculated numerically as

$$I_\mu(X, \cos \theta^*, \phi) \simeq \frac{\ln 10 (\log E_u - \log E_l)}{N} \sum_{\{i\}} E_{\mu 0i} \frac{dN_{\mu 0}(E_{\mu 0i}, \cos \theta_i^*)}{dE_{\mu 0i} d\Omega}. \quad (\text{A3})$$

The symbol $\{i\}$ denotes a subset of simulated events corresponding to surviving muons. Information of X and ϕ on the right-hand-side of Eq. (A3) are defined as inputs in the simulation and are not shown formally. The probability function $P(E_{\mu 0}, X, \theta^*, \phi)$ is not explicitly computed in Eq. (A3) by design. The simplicity of this algorithm translates to saving in memory. Since the probability function is not computed explicitly for each combination of $E_{\mu 0}$, θ and ϕ , it is essential that the generation of these integration variables is uniform so that the probability function is calculated implicitly when the sum is divided by N in Eq. (A3). As a test of the accuracy of present method, it will be shown later that the uniform generation of integration variables gives exactly the same results as those calculated by the Gaussian quadrature method in the case of ground level muons.

Vertical muon intensity and average energy are easily computed as

$$I_\mu^v(h) \simeq \frac{\ln 10 (\log E_u - \log E_l)}{N} \sum_{\{i\}} E_{\mu 0i} \frac{dN_{\mu 0}(E_{\mu 0i}, \cos \theta_i^* = 1)}{dE_{\mu 0i} d\Omega}, \quad (\text{A4})$$

$$E_\mu^v(h) \simeq \frac{\ln 10 (\log E_u - \log E_l)}{N I_\mu^v(h)} \sum_{\{i\}} E_{\mu i} E_{\mu 0i} \frac{dN_{\mu 0}(E_{\mu 0i}, \cos \theta_i^* = 1)}{dE_{\mu 0i} d\Omega}. \quad (\text{A5})$$

Vertical muon intensity in standard rock simulated with Eq. (A4) is compared against experimental data in Figs. 2 and 3. In reality, standard rock does not exist and is generally not an exact match of real rock profiles in real experiments. When measurements are converted from real rocks to standard rock, there are always some questions regarding the accuracy of the conversion schemes. For this reason, Figs. 2 and 3 should not be taken as absolute tests of the accuracy of MUSIC and the present integration method but merely a relative point of reference. Despite of the question of the accuracy of the standard rock experimental data, it is shown in Fig. 3 that the ratios of calculated and experimental vertical intensity scatter symmetrically around unity so that the simulated results are said to agree with experiments at large. It should be noted that vertical intensity is merely an approximate test and is not the central focus of the present work. Integrated intensity on the other hand is really what is needed for the calculation of muon overburden in realistic calculations. Integrated muon intensity and average energy can be implemented in a similar way as Eqs. (A4)–(A5),

$$J_\mu \simeq \frac{\Omega \ln 10 (\log E_u - \log E_l)}{N} \sum_{\{i\}} E_{\mu 0i} \frac{dN_{\mu 0}(E_{\mu 0i}, \cos \theta_i^*)}{dE_{\mu 0i} d\Omega}, \quad (\text{A6})$$

$$E_\mu \simeq \frac{\Omega \ln 10 (\log E_u - \log E_l)}{N J_\mu(h)} \sum_{\{i\}} E_{\mu i} E_{\mu 0i} \frac{dN_{\mu 0}(E_{\mu 0i}, \cos \theta_i^*)}{dE_{\mu 0i} d\Omega}, \quad (\text{A7})$$

where Ω is the solid angle over the integrated hill profile. The average muon energy E_μ can be organized into $M = 500$ bins along $\log E_\mu$. The subscript j denotes the j -th bin. The numerical implementation of Eq. (21) is

$$\frac{dJ_\mu}{dE_{\mu j}} \simeq \frac{\Omega M}{N} \sum_{i=1}^{N(E_{\mu j})} \frac{E_{\mu 0i}}{E_{\mu j}} \frac{dN_{\mu 0}(E_{\mu 0i}, \cos \theta_i^*)}{dE_{\mu 0i} d\Omega}. \quad (\text{A8})$$

Information of the survival probability is hidden in $N(E_{\mu j})$ that gives the number of surviving muons in the j -th bin. As a consistency check,

$$J_\mu \simeq \frac{\ln 10(\log E_u - \log E_l)}{M} \sum_{j=1}^M E_{\mu j} \frac{dJ_\mu(h)}{dE_{\mu j}}, \quad (\text{A9})$$

and

$$E_\mu \simeq \frac{\ln 10(\log E_u - \log E_l)}{M \tilde{J}_\mu(h)} \sum_{i=1}^M E_{\mu i}^2 \frac{dJ_\mu(h)}{dE_{\mu j}} \quad (\text{A10})$$

must agree with those obtained by Eq. (A6) and (A7). Angular and double differential distributions are constructed in similar ways. For instance, the $\cos \theta$ distribution can be constructed as

$$\frac{dJ_\mu}{d \cos \theta_j} = \frac{\Omega}{2} \frac{M \ln 10(\log E_u - \log E_l)}{N} \sum_{i=1}^{N(\cos \theta_j)} E_{\mu 0i} \frac{dN_{\mu 0}(E_{\mu 0i}, \cos \theta_j^*)}{dE_{\mu 0i} d\Omega}. \quad (\text{A11})$$

The factor $\Omega/2$ in Eq. (A11) gives the proper normalization so that the integration over $-1 \leq \cos \theta \leq 1$ gives the correct solid angle Ω . Similarly the ϕ distribution is given as

$$\frac{dJ_\mu}{d\phi_j} = \frac{\Omega}{2\pi} \frac{M \ln 10(\log E_u - \log E_l)}{N} \sum_{i=1}^{N(\phi_j)} E_{\mu 0i} \frac{dN_{\mu 0}(E_{\mu 0i}, \cos \theta_i^*)}{dE_{\mu 0i} d\Omega}. \quad (\text{A12})$$

In the case of Eq. (A12), the normalization factor is $\Omega/2\pi$ so that the integration around $0 \leq \phi < 2\pi$ gives the correct solid angle Ω . There is a subtlety involving the θ distribution. Since $\cos \theta$ (not θ) is uniformly generated in the present method, uniform binning in θ leads to the wrong distribution. The correct bin width must be inversely proportional to $\cos \theta$ or, more precisely speaking, equals $M/(N \cos \theta)$. The factor of $1/\cos \theta$ exactly cancels the factor of $\cos \theta$ of the Jacobian so that the θ distribution is

$$\frac{dJ_\mu}{d\theta_j} = \frac{\Omega}{\pi} \frac{M \ln 10(\log E_u - \log E_l)}{N} \sum_{i=1}^{N(\theta_j)} E_{\mu 0i} \frac{dN_{\mu 0}(E_{\mu 0i}, \cos \theta_j^*)}{dE_{\mu 0i} d\Omega}. \quad (\text{A13})$$

Double differential distributions of various kinds can be constructed using the same logic.

Exact calculation of the slant depth X is generally impossible for any arbitrary latticized hill profile. Fortunately simulated energy loss by MUSIC is not very sensitive to small changes in X so that an approximation can be made. Figure 14 illustrates the binning strategy of X in the $\theta - \phi$ space. The idea is to partition the solid angle into regions of nearest neighbors. Each region has the same value of X . Evenly generated θ and ϕ pick out an approximate value of X in the corresponding nearest neighborhood. There is a certain amount of computation overhead in pre-processing the partitions. When the number of simulated events is sufficiently large, the overhead of partitioning is still more cost-effective than a real-time search per event. Due to the irregularity of the hill profile, any given differential solid angle in the upper hemisphere may traverse disconnected parts of the hill profile. For this reason, the code must incorporate a mechanism to pick out the appropriate slant depth X . It can be easily implemented by simply keeping only the minimum value of X for any given grid in a latticized $\theta - \phi$ space. On ground level, muons do not need to be propagated by MUSIC so that Eqs. (16) and (17) can be integrated by Gaussian quadrature and by setting $P(E_{\mu 0}, X, \theta^*, \phi) = 1$ in the integrand. Figures 15–16 and Table IV show that results generated by the present Monte Carlo method agree exactly with those calculated by the Gaussian quadrature method.

Assuming that pairs of $\cos \theta$, ϕ are uniformly generated N times and that the generation is truly random, the hemispherical Ω would have been partitioned into N segments uniformly. In that case $d\mathbf{A} \cdot \hat{r} = A_0 \hat{r} \cdot \hat{r}_0 / N$ so that the integral of the differential projected surface areas is simply the sum of the segments corresponding to the surviving muons. In other words, for any given \hat{r} , $\int d\mathbf{A} \cdot \hat{r} = A_0 \langle P \rangle \hat{r} \cdot \hat{r}_0$ where $\langle P \rangle$ is the pseudo survival probability of muons. A real survival probability of muons can only be computed by generating muons according to the sea level muon distribution and by propagating them through rock. In the present method, muons are generated uniformly in $E_{\mu 0}$, $\cos \theta$ and ϕ so that $\langle P \rangle$ does not have any natural meaning other than the ratio of the surviving muons to the generated muons. Naïvely $\langle P \rangle$ may be set to the ratio of the number of surviving muons n to the generated muons N according to this definition. However a more careful look reveals that n increases as the muon energy threshold E_l

is raised in the simulation. The reason is simply that more highly energetic muons generally have a better chance of surviving through rock. For this reason, a proper definition of $\langle P \rangle$ must be independent of E_l and is founded to be

$$\langle P \rangle = \frac{n}{N} \frac{\log E_u - \log E_l}{\log E_u - \log m_\mu}. \quad (\text{A14})$$

$\langle P \rangle$ defined in Eq. (A14) is effectively independent of E_l because n varies inversely with $\log E_l$. On the other hand, n decreases when E_u decreases because less highly energetic muons are generally less likely to survive through rock. Unfortunately there is no simple way to rescale $\langle P \rangle$ in this case. For an accurate calculation of $R_\mu(h)$, it is recommended that E_u is kept at 10^6 GeV. With $\langle P \rangle$ in place, Eq. (20) can be implemented as

$$R_\mu \simeq \frac{A_0 \langle P \rangle \Omega \ln 10 (\log E_u - \log E_l)}{N} \sum_{\{i\}} \hat{r}_i \cdot \hat{r}_{0i} E_{\mu 0i} \frac{dN_{\mu 0}(E_{\mu 0i}, \cos \theta_i^*)}{dE_{\mu 0i} d\Omega}. \quad (\text{A15})$$

The dot products $\hat{r}_i \cdot \hat{r}_{0i}$ are generated randomly inside the entire detector volume and not just at the center. This strategy renders a fairer sampling of the detector geometry. On the other hand, the hill profile is defined with respect to the origin which is normally set at the center of the detector because the generation of slant depth X is not easily managed when the origin moves. Since MUSIC is relatively insensitive to small change in X and the size of the detector is generally small compared to the mountain profile, generation of X from the center of the detector is adequate.

-
- [1] Y. Koshio, “Study of Solar Neutrinos at Super Kamiokande”, Ph. D. thesis, Tokyo University (1998).
 - [2] Y. Fukuda *et al.*, Phys. Rev. Lett. **82** (1999), 2644.
 - [3] Y. Gando *et al.*, Phys. Rev. Lett. **90**, 171302 (2003).
 - [4] A. Habig, “An Indirect Search for WIMPS with Super-Kamiokande”, Proceedings of ICRC 2001, Copernicus Gesellschaft (2001).
 - [5] P. Antonioli, C. Ghatti, E. V. Korolkova, V. A. Kudryavtsev and G. Sartorelli, Astroparticle Physics, **7**, 357 (1997).
 - [6] V. A. Kudryavtsev, E. V. Korolkova and N. J. C. Spooner, Phys. Lett. B, **471** (1999), 251-256.
 - [7] B. Rossi, Reviews of Modern Physics, **20** (July 1948), 537.
 - [8] T. K. Gaisser and T. Stanev, “Cosmic Rays,” Review of Particle Physics, edited by L. Alvarez-Gaumé *et al.*, Physics Letters, **B592**, 228 (2004).
 - [9] M. Aglietta *et al.* (The LVD Collaboration), Phys. Rev. D **58**, 092005 (1998).
 - [10] M. Aglietta *et al.* (The LVD Collaboration), Phys. Rev. D **60**, 112001 (1999).
 - [11] H. Bichsel, D. E. Groom and S. R. Klein, “Passage of Particles through Matters,” Review of Particle Physics, edited by L. Alvarez-Gaumé *et al.*, Physics Letters, **B592**, 228 (2004).
 - [12] A. Dar, Phys. Rev. Lett. **51** (1983), 227.
 - [13] J. W. Elbert, Proceedings of Cosmic Ray Conference, **1**, Denver (1973), 213-218.
 - [14] T. K. Gaisser and M. Honda, Annual Review of Nuclear and Particle Science, **52** (December 2002), 153-199.
 - [15] G. Ingelman and M. Thunman, Phys. Rev. D **54** (1996), 4385.
 - [16] D. Chirkin, hep-ph/0407078.
 - [17] D. P. Bhattacharyya, J. Phys. A **6** (1973), 582; D. P. Bhattacharyya, J. Phys. A **7** (1974), 158.
 - [18] M. Motoki *et al.*, Astroparticle Phys. **19** (2003), 113-126.
 - [19] P. Hansen, T. K. Gaisser, T. Stanev and S. J. Sciutto, Phys. Rev. D **71**, 083012 (2005).
 - [20] M. P. De Pascale *et al.*, J. Geophys. Res. **98**, 3501 (1993).
 - [21] O. C. Allkofer, K. Carstensen, and W. D. Dau, Phys. Lett. **B36**, 425 (1971).
 - [22] O. C. Allkofer, K. Carstensen, and W. D. Dau, Proc. 12th Int. Conf. on Cosmic Rays, 1314, University of Tasmania, Hobart, 1971.
 - [23] B. C. Rastin, J. Phys. **G10**, 1609 (1984).
 - [24] C. A. Ayre *et al.*, J. Phys. **G1**, 584 (1975).
 - [25] J. Kremer *et al.*, Phys. Rev. Lett. **83**, 4241 (1999).
 - [26] H. Jokisch, K. Carstensen, W. D. Dau, H. J. Meyer and O. C. Allkofer, Phys. Rev. D **19**, 1368 (1979).
 - [27] P. K. F. Grieder, Cosmic Rays at Earth, Elsevier, Amsterdam, 2001.
 - [28] V. Agrawal, T. K. Gaisser, P. Lipari and T. Stanev, Phys. Rev. D **53**, 1314 (1996).
 - [29] M. G. Thompson, “Energetic Muons,” Cosmic Rays at Ground Level, edited by A. W. Wolfendale, Institute of Physics Press, London, 1973.
 - [30] P. J. Hayman and A. W. Wolfendale, Proc. Phys. Soc. **80** (1962), 710.
 - [31] V. A. Kudryavtsev, *et al.*, Nuclear Instrumentation and Methods, **A505**: 683 (2003); hep-ex/0303007.
 - [32] E. V. Bugaev, A. Misaki, V. A. Naumov, T. S. Sinegovskaya, S. I. Sinegovsky and N. Takahashi, Phys. Rev. D, **58**, 054001 (1998).
 - [33] M. Fukugita and A. Suzuki, “Physics and Astrophysics of Neutrinos,” Springer-Verlag, Tokyo (1994), 415.

- [34] V. Galouchko, <http://field.hypermart.net>.
- [35] A. Baldini *et al.*, “Geology at the CHOOZ site”, CHOOZ internal note (1994), (unpublished).
- [36] M. Apollonio *et al.*, Eur. Phys. J. **C** (2003), 331.
- [37] M. Nakahata, “Kamiokande and Super-Kamiokande” AAPPs Bulletin, **13**, 4 (August 2003), 7-12.
- [38] K. Eguchi, *et al.*, Phys. Rev. Lett. **90**, 021802 (2003).
- [39] D. Dwyer, KamLAND internal page.
- [40] T. Araki, KamLAND internal page.
- [41] A. A. Lagutin, A. G. Tyumentsev and A. V. Yushkov, J. Phys. G **30** (2004), 573-596.
- [42] W. H. Press, S. A. Teukolsky, W. T. Vetterling and B. P. Flannery, Numerical Recipes in Fortran, Cambridge University Press, 1992.
- [43] R. W. Flint, R. B. Hicks and S. Standil, Canadian J. Phys. **50**, 843 (1972).
- [44] B. G. Wilson, Canadian J. Phys. **37**, 19 (1959).

FIGURES

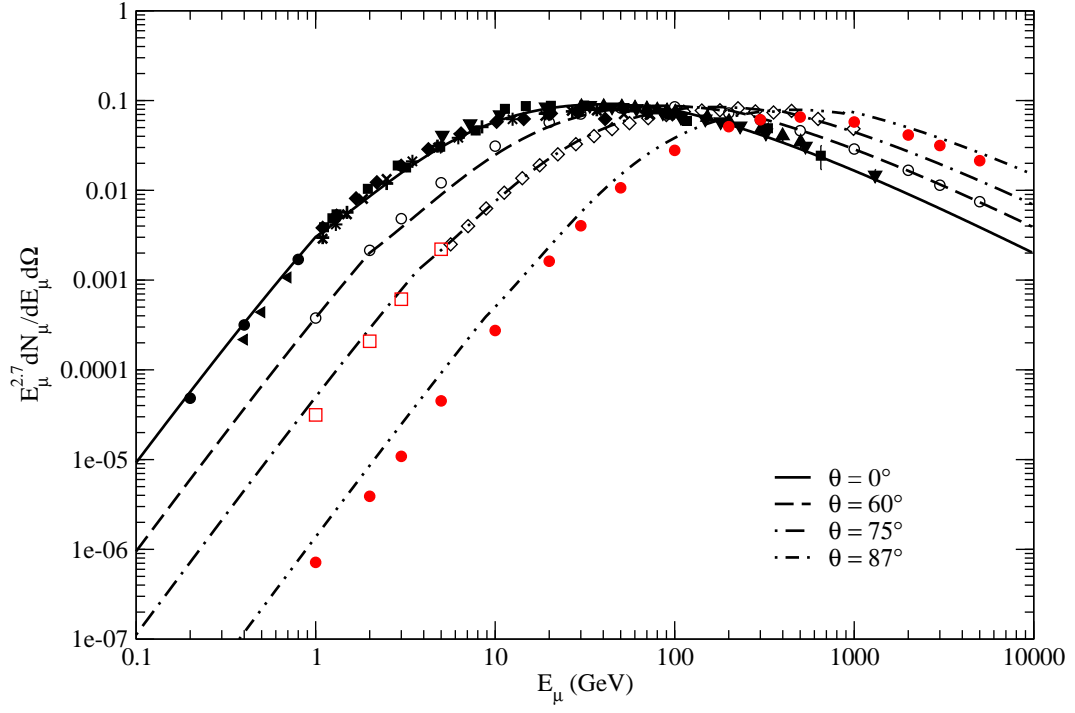


FIG. 1: Fits of the modified Gaisser parameterization to experimental data in the low energy regime between $\theta = 0$ and $\theta = 87^\circ$. The experimental data are taken from References [8], [20]–[30]. The modified Gaisser parameterization is given by Eqs. (3)–(7) and (9)–(10).

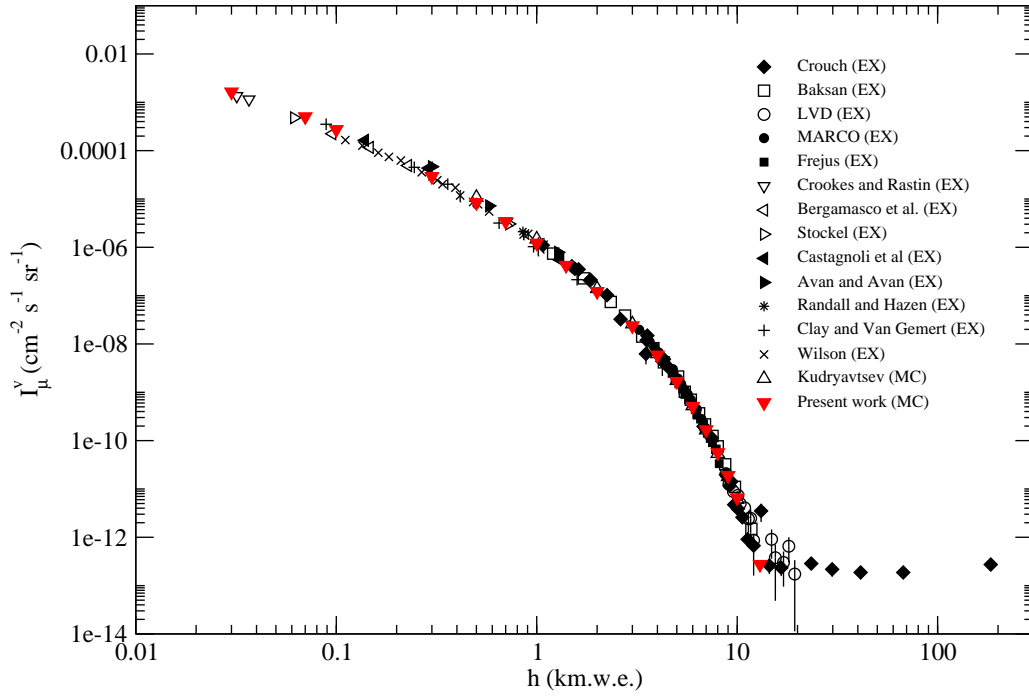


FIG. 2: Average vertical muon intensity $I_\mu^v(h)$ versus vertical depth h beneath a flat surface in standard rock. Experimental and simulated data are labeled by EX and MC respectively. The experimental data of the flat surface overburden are taken from References [8, 32] and the simulated data by Kudryavtsev *et al.* from Reference[31]. The number of simulated events per data point in this figure is $N = 10^6$. The set of simulated data labeled as “Present work” is generated from the modified Gaisser parameterization of the surface muon intensity in Eqs. (4)–(7).

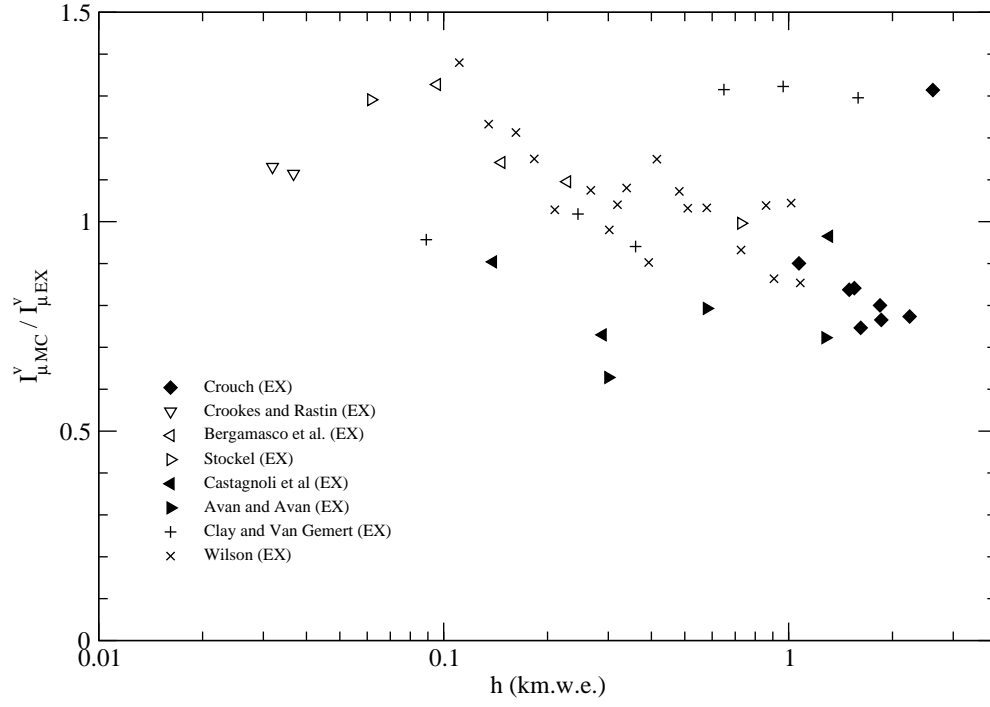


FIG. 3: Ratio of simulated vertical muon intensity $I_{\mu}^v(h)_{MC}$ over the experimental vertical muon intensity $I_{\mu}^v(h)_{EX}$ versus shallow depth h beneath a flat surface in standard rock. The experimental data of the flat surface overburden are taken from References [8, 32]. The number of simulated events per data point in this figure is $N = 10^6$. The simulated data are generated from the modified Gaisser parameterization incorporating Eqs. (4)–(7).

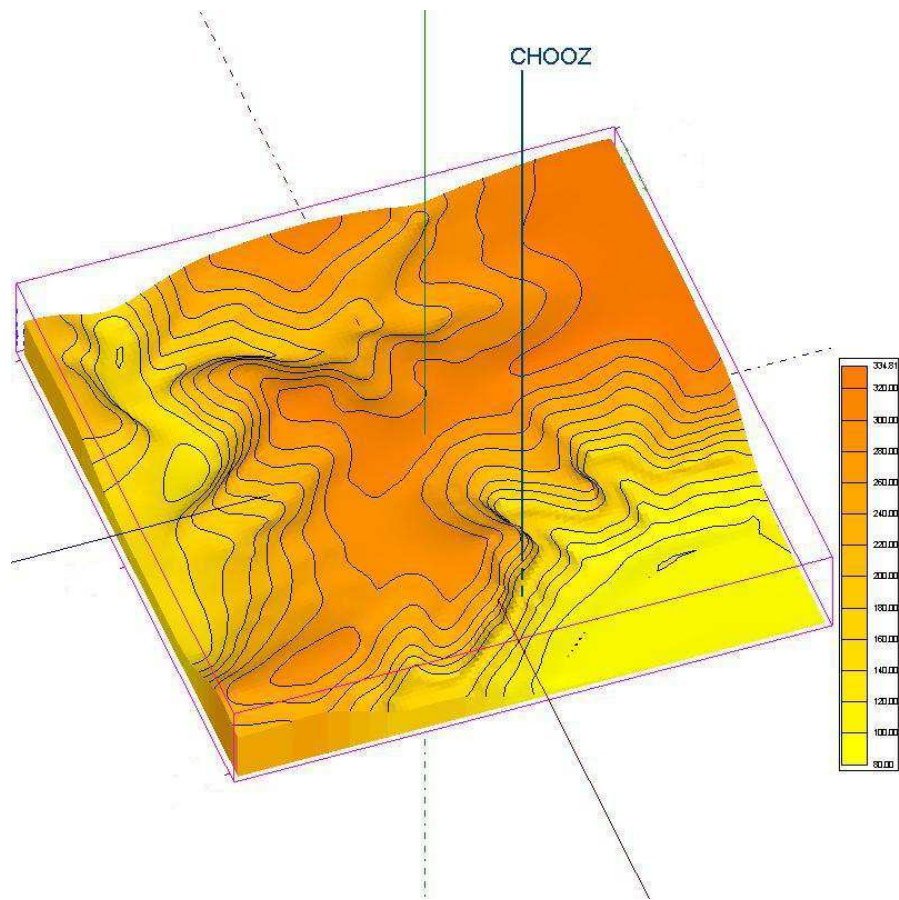


FIG. 4: A visualization of the 3D topological profile of the Ardennes Mountains over the CHOOZ site generated by 3DField from a 2D contour map.

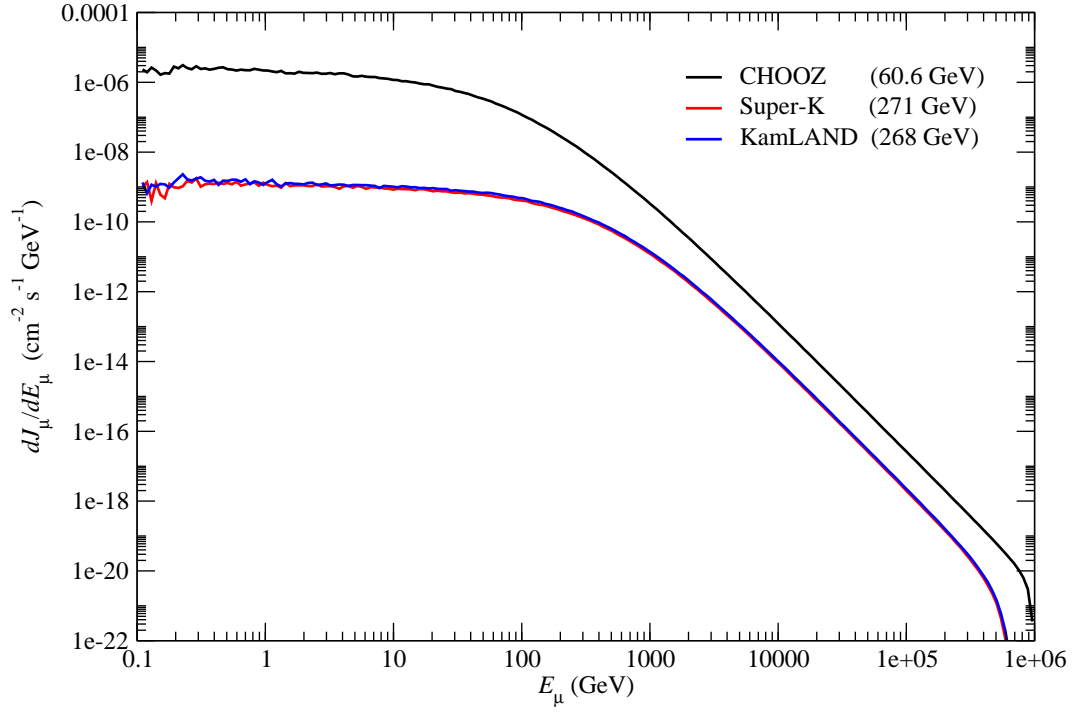


FIG. 5: Integrated muon intensity distribution at Super-K, KamLAND and CHOOZ. The number of energy bins is $M = 500$. The total number of simulated events is 5×10^6 . The average muon energies of the three sites are quoted in the legend.

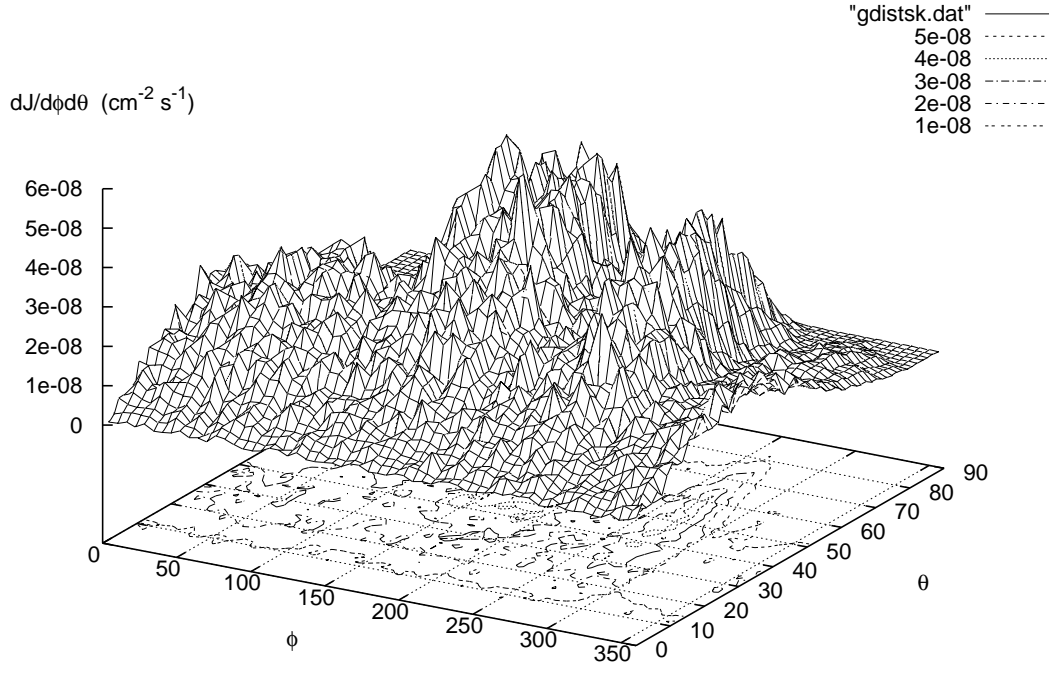


FIG. 6: Angular distribution of final muons at Super-K. The total number of simulated events is 5×10^6 . The Super-K digital map defines $\phi = 0$ to be along the northerly axis and the sense of rotation to be clockwise.

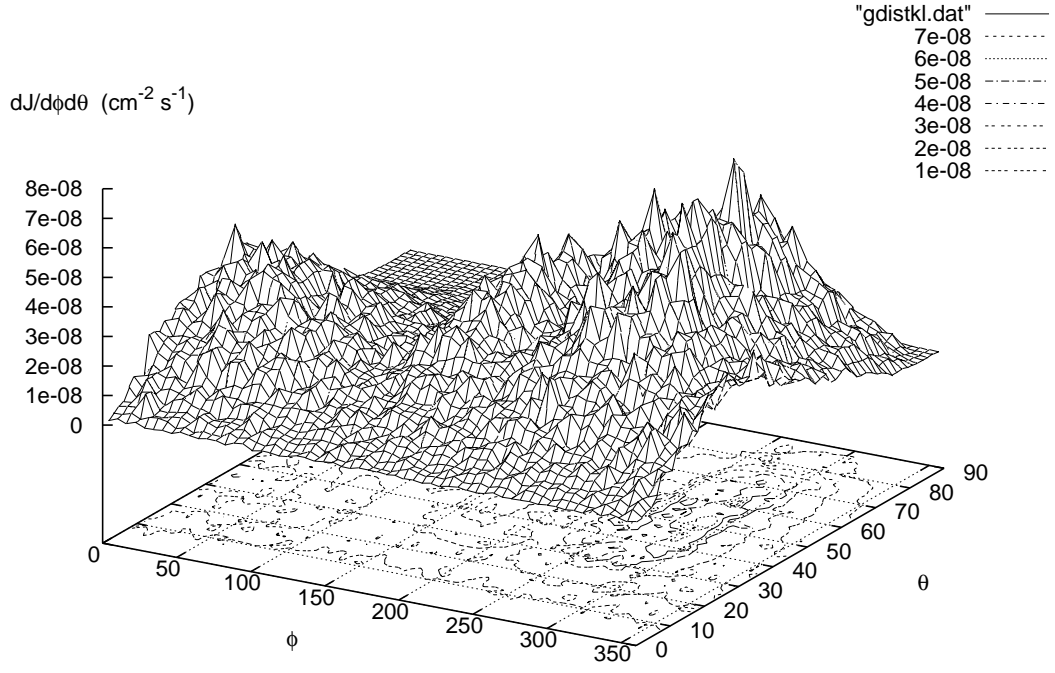


FIG. 7: Angular distribution of final muons at KamLAND. The total number of simulated events is 5×10^6 .

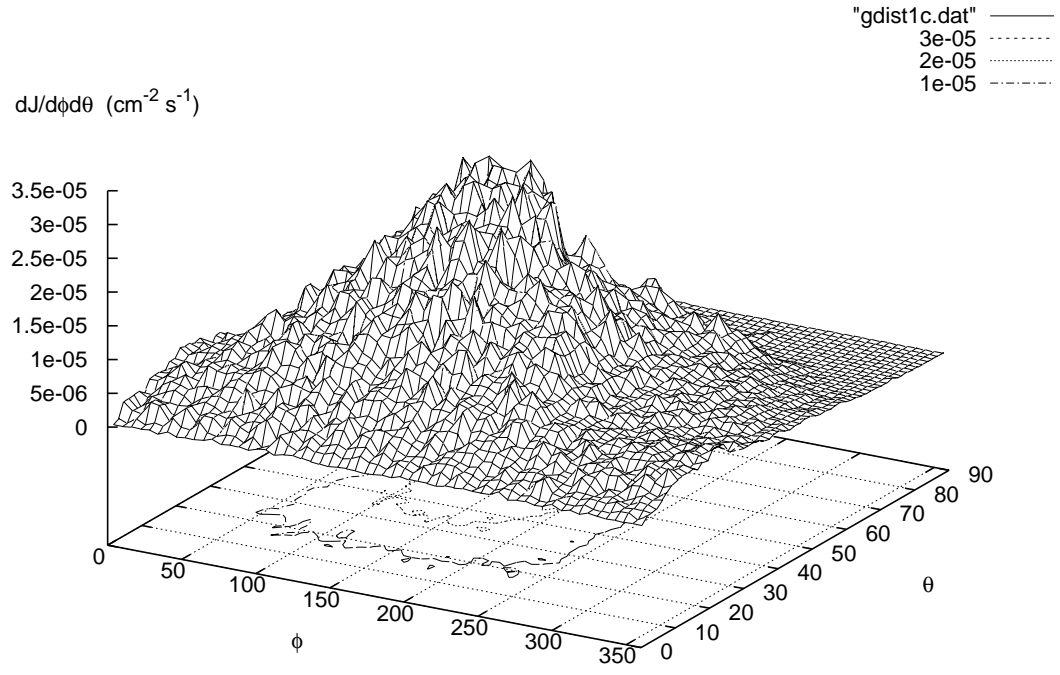


FIG. 8: Angular distribution of final muons at CHOOZ. The total number of simulated events is 5×10^6 .

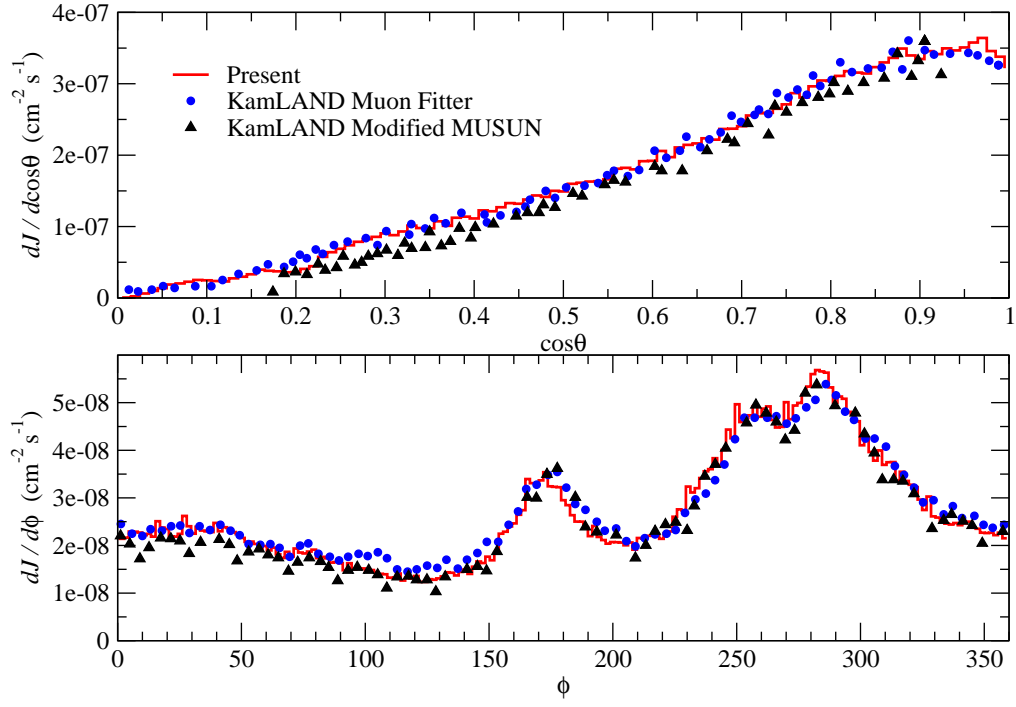


FIG. 9: Comparisons of the $\cos\theta$ and ϕ distributions of final muons at KamLAND. The total number of simulated events of the present **MUSIC** simulation is 5×10^6 . The muon fitter results [39] represent actual experimental data. The modified **MUSUN** simulation [40] is a standard rock calculation while the present simulation is an exact calculation based on the Ikenoyama rock composition. Both the muon fitter and modified **MUSUN** results are rescaled from arbitrary units to fit the present results.

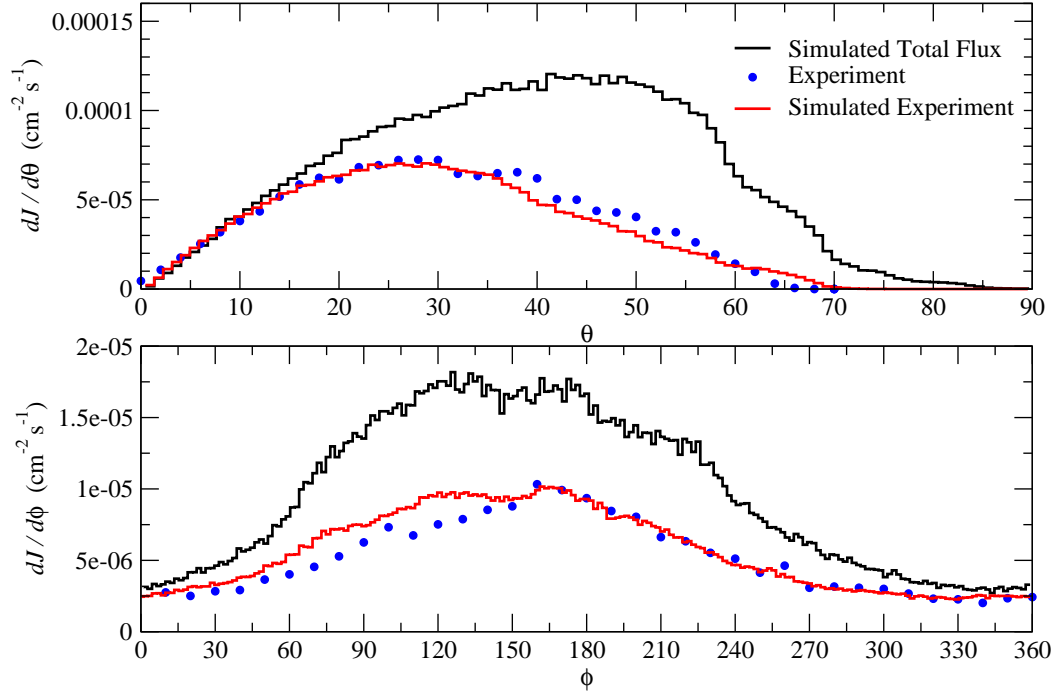


FIG. 10: Comparisons of the θ and ϕ distributions of final muons at CHOOZ. The total number of simulated events of the present MUSIC simulation is 5×10^6 . “Simulated Total Flux” refers to the simulated muon flux integrated over the entire hemispherical solid angle. The total flux is binned to generate the angular distributions. “Simulated Experiment” is the simulated muon flux integrated over a limited range of solid angle described by the geometry of the RPC plates used in the cosmic ray experimental setup on the CHOOZ site. Both the experimental and simulated experimental results are rescaled such that the small angle parts of all three θ distributions agree.

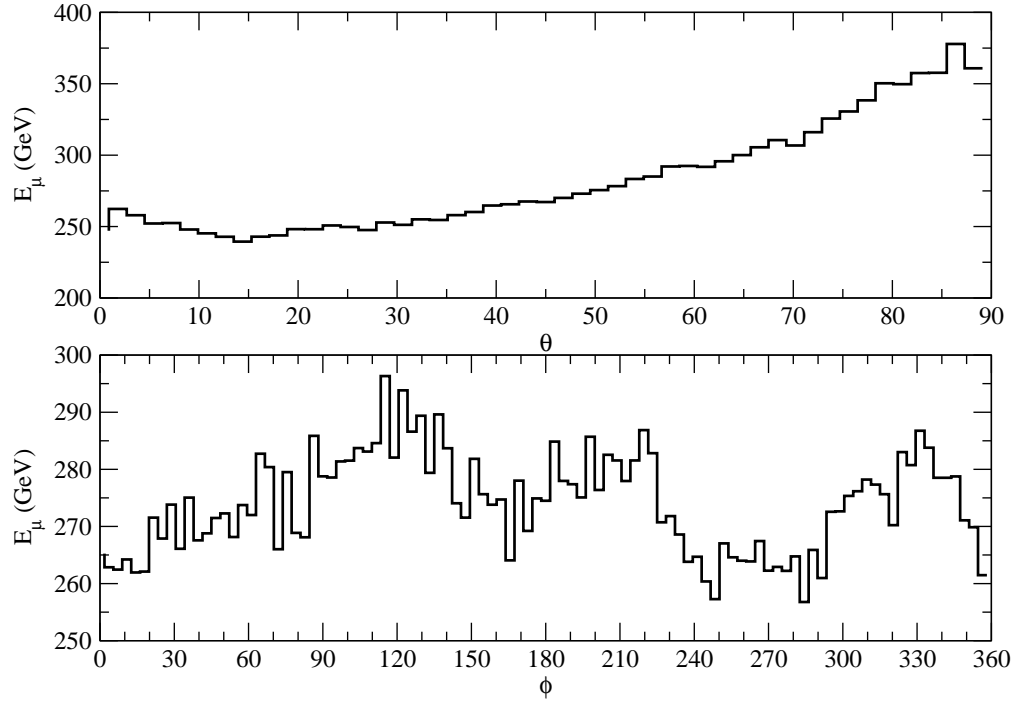


FIG. 11: Average muon energy E_μ versus θ and ϕ at KamLAND. The total number of simulated events is 5×10^6 .

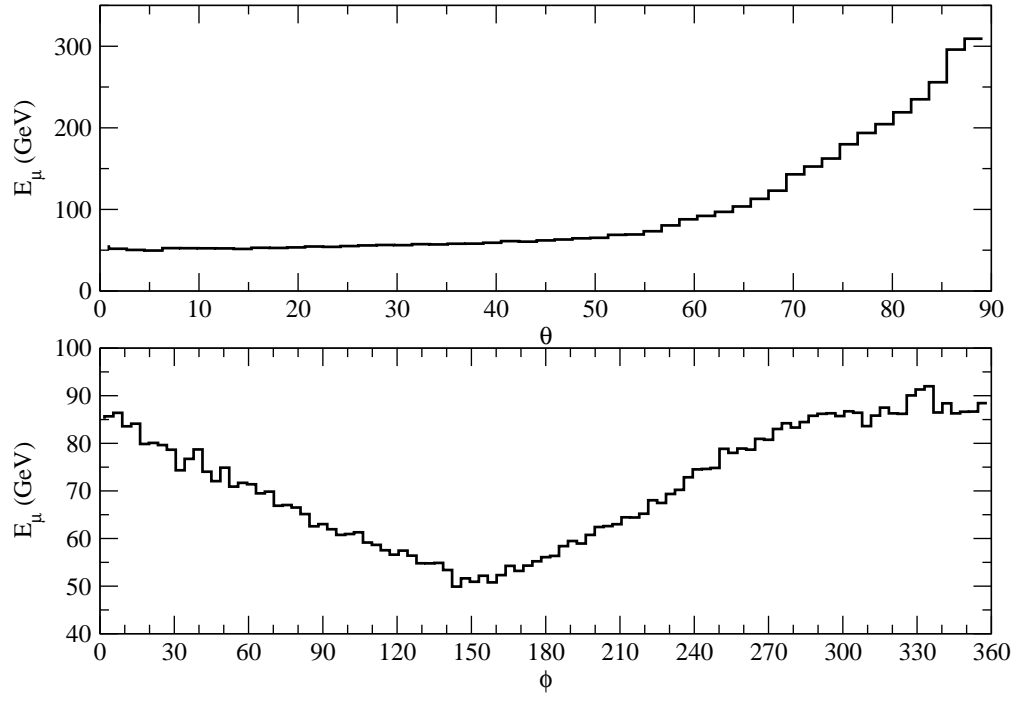


FIG. 12: Average muon energy E_μ versus θ and ϕ at CHOOZ. The total number of simulated events is 5×10^6 .

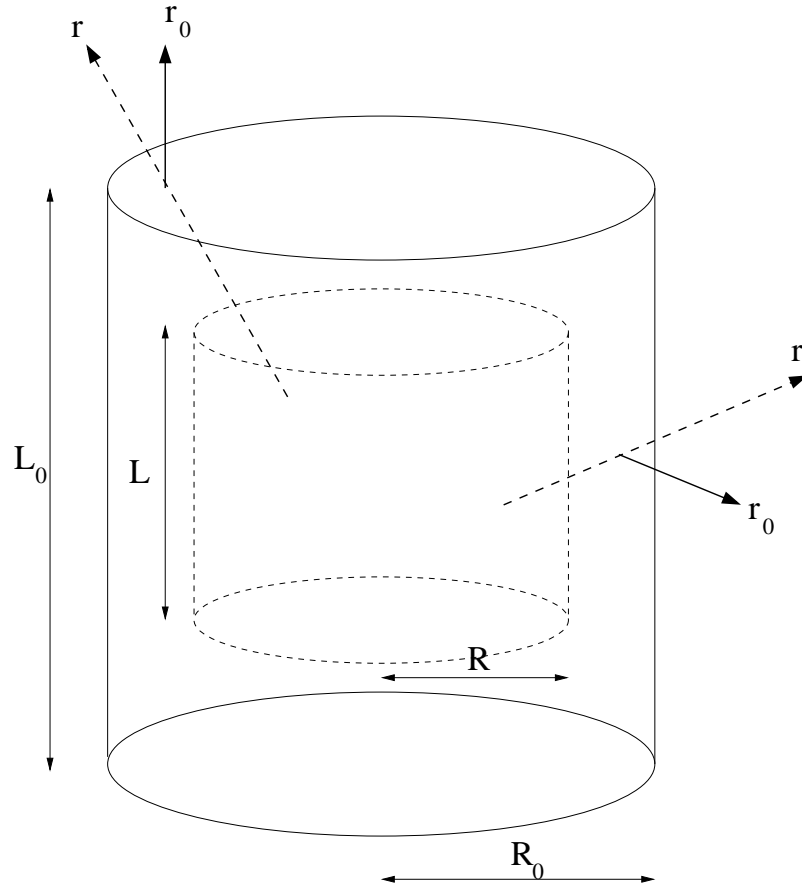


FIG. 13: A sketch of a vertical cylindrical detector. The inner volume is indicated by dotted lines which is taken to be cylindrical for Super-K and CHOOZ but spherical for KamLAND.

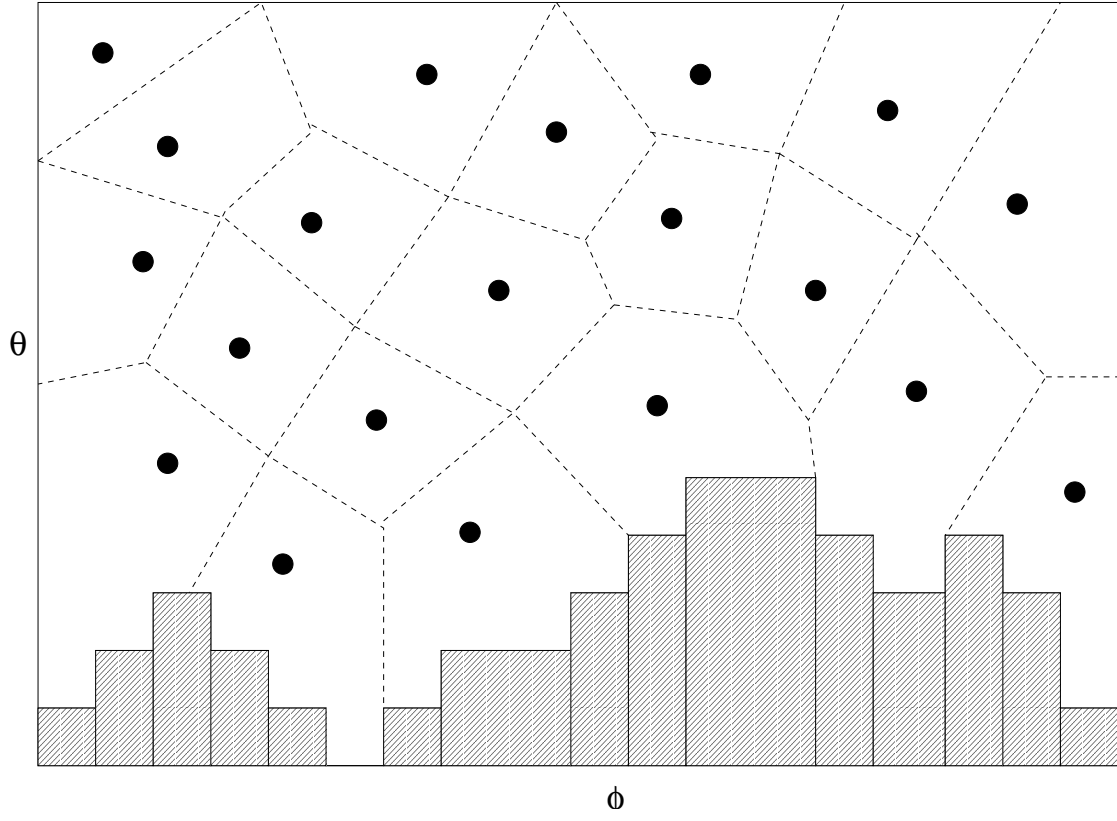


FIG. 14: An illustration of the binning strategy of slant depth X in the $\theta - \phi$ space. The bars represents regions of the solid angle corresponding to the edges of a 3D topographical map and is blocked from the random generation of θ and ϕ . The black dots represent the original lattice sites from a latticized hill profile. The dotted lines partition the remaining solid angle into regions of nearest neighbors.

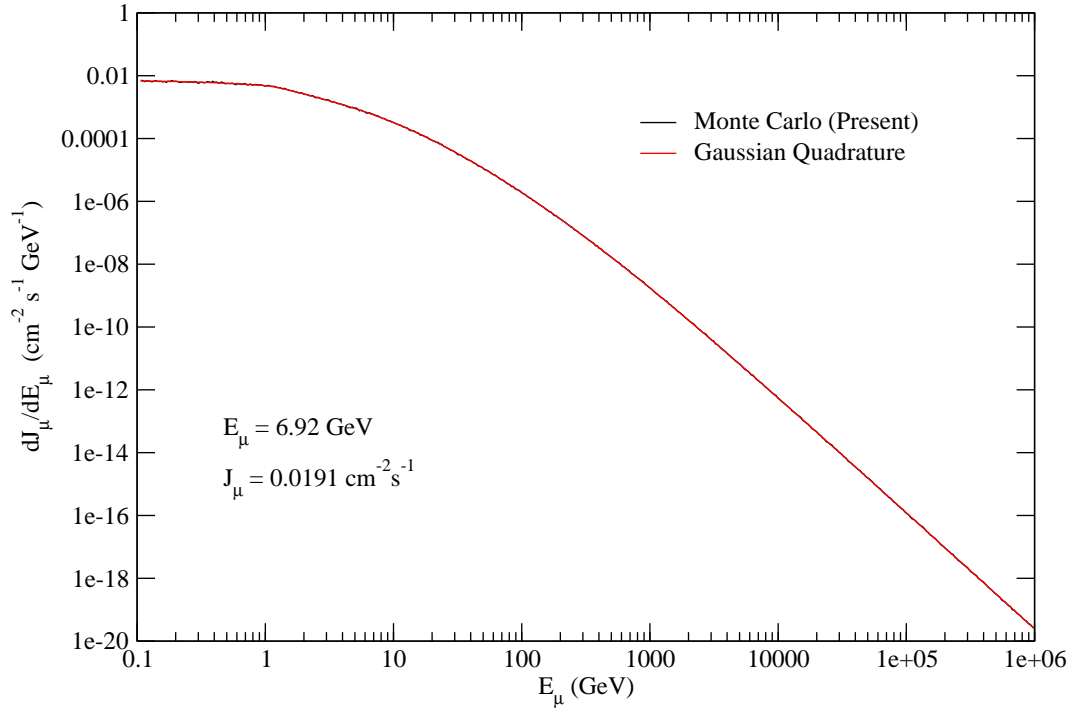


FIG. 15: Integrated muon flux versus muon energy on ground level. The angular integration is taken over the the entire hemisphere. Experimental data support the feature that the energy spectrum for $E_\mu < 1 \text{ GeV}$ is almost flat [8].

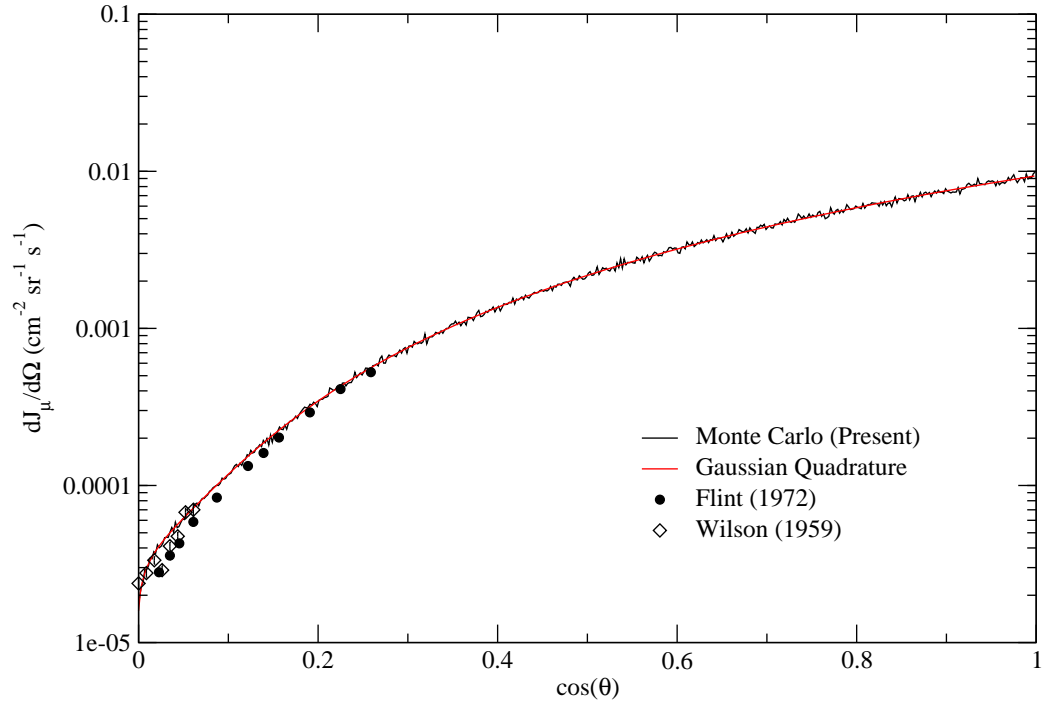


FIG. 16: Integrated muon flux versus the zenith angle on ground level. The energy integration is taken over the range $0.106\text{--}10^6$ GeV. The experimental data are taken from References [43, 44].

TABLES

TABLE I: Integrated muon intensity J_μ and energy E_μ versus vertical depth h from a flat surface in standard rock. Results labeled “Sheffield” are taken from Reference [31] that uses the original Gaisser parameterization and **MUSIC**. Results labeled “KSU” present this work using the modified Gaisser parameterization in Eqs. (4)–(7) and **MUSIC**. The initial muon energy for vertical depth ($300 \leq h \leq 2000$) mwe is ($0.106 < E_{\mu 0} \leq 10^6$) GeV and for ($2000 < h \leq 10000$) mwe is ($0.106 < E_{\mu 0} \leq 10^7$) GeV. The number of simulated events is 10^6 .

h (mwe)	Sheffield J_μ ($\text{cm}^{-2}\text{s}^{-1}$)	KSU J_μ ($\text{cm}^{-2}\text{s}^{-1}$)	Sheffield E_μ (GeV)	KSU E_μ (GeV)
500	1.70×10^{-5}	1.71×10^{-5}	97	97
1000	2.20×10^{-6}	2.21×10^{-6}	157	158
2000	1.81×10^{-7}	1.81×10^{-7}	236	236
3000	2.94×10^{-8}	2.95×10^{-8}	285	284
4000	6.33×10^{-9}	6.34×10^{-9}	316	313
5000	1.58×10^{-9}	1.57×10^{-9}	337	339
6000	4.30×10^{-10}	4.21×10^{-10}	351	345
7000	1.24×10^{-10}	1.26×10^{-10}	361	365
8000	3.73×10^{-11}	3.61×10^{-11}	369	356
9000	1.15×10^{-11}	1.14×10^{-11}	375	373
10000	3.65×10^{-12}	3.61×10^{-12}	380	363

TABLE II: Chemical composition of the Ikenoyama and Ardennes rock in elemental percentage. The Ardennes rock composition is the average of several samples. The CHOOZ rock data are approximate values only. Details are documented in an internal note [35].

Chemical formula	Ikenoyama %	Ardennes %
Si O ₂	60.70	58
Ti O ₂	0.31	
Al ₂ O ₃	17.39	19
Fe ₂ O ₃	1.10	
Fe O	1.22	17
Mn O	0.15	
Mg O	0.93	4
Ca O	6.00	
Na ₂ O	6.42	
K ₂ O	3.47	2
P ₂ O ₅	0.18	
H ₂ O	0.97	
S	0.01	
C O ₂	0.96	

TABLE III: Average muon energy E_μ , muon flux J_μ , the muon rate inside the tank R_μ^t and the muon rate inside the inner detector volume R_μ^i for Super-K, KamLAND and CHOOZ. The inner detector of Super-K is a cylinder and that of KamLAND is a balloon. The muon rate inside the CHOOZ inner detector is not simulated.

Site	E_μ (GeV)	J_μ ($\text{cm}^{-2}\text{s}^{-1}$)	R_μ^t (Hz)	R_μ^i (Hz)
Super-K	271 ± 2	$(1.48 \pm 0.04) \times 10^{-7}$	2.438 ± 0.004	1.828 ± 0.003
KamLAND	268 ± 2	$(1.70 \pm 0.05) \times 10^{-7}$	0.676 ± 0.001	0.246 ± 0.001
CHOOZ	60.6 ± 0.4	$(6.12 \pm 0.07) \times 10^{-5}$	30.5 ± 0.2	-

TABLE IV: Comparisons of muon flux and average energy on the ground level. The experimental values of muon flux is taken from Reference [27]. The momentum cut-off of the muon flux measurement is 0.35 GeV. The low total energy cut-off of the present calculations is 0.106 GeV. The quoted experimental value [8] of vertical muon energy is 4 GeV. The simulated value is 4.19 GeV.

Method	J_μ ($\text{cm}^{-2} \text{s}^{-1}$)	E_μ (GeV)
Monte Carlo	1.91×10^{-2}	6.92
Gaussian Quadrature	1.90×10^{-2}	6.95
Experiments	$(1.90 \pm 0.12) \times 10^{-2}$	